Indoor 3-D Radar Imaging for Low-RCS Analysis

PIERRE MINVIELLE
PIERRE MASSALOUX
CESTA, DAM, CEA, Le Barp, France

JEAN-FRANÇOIS GIOVANNELLI
University Bordeaux, CNRS, BINP, Talence, France

An original 3-D radar imaging system is presented for radar cross section (RCS) analysis, i.e., to identify and characterize the radar backscattering components of an object. Based on a 3-D spherical experimental setup, where the residual echo signal is more efficiently reduced in the useful zone, it is especially adapted to deal with low-RCS analysis. Due to a roll rotation, the electric field direction varies concentrically while the scattered data are collected. To overcome this issue, a specific 3-D radar imaging algorithm is developed. Based on fast regularization inversion, more precisely the minimum norm least squares solution, it manages to determine, from a single pass collection, three huge 3-D scatterer maps at once, which correspond to HH, VV, and HV polarizations at emission and reception. The algorithm is applied successfully to real X-band datasets collected in the accurate 3-D spherical experimental layout, from a metallic cone with patches and an arrow shape. It is compared with the conventional 3-D polar format algorithm where the scatterer information is irretrievably mixed-up.

Manuscript received March 2, 2016; revised October 28, 2016; released for publication January 5, 2017. Date of publication February 9, 2017; date of current version April 27, 2017.

DOI. No. 10.1109/TAES.2017.2667378

Refereeing of this contribution was handled by K. S. Kulpa.

Authors' addresses: P. Minvielle and P. Massaloux are with CESTA, DAM, CEAF-3114, Le Barp, France, E-mail: (pierre.minvielle@cea.fr); J.-F. Giovannelli is with IMS, University Bordeaux, CNRS, BINP, F-33400 Talence, France, E-mail: (pierre.massaloux@cea.fr; jean-francois.giovannelli@u-bordeaux.fr).

I. INTRODUCTION

Radar imaging consists in making a map or image of the spatial distribution of reflectivity or backscattering of an object or scene from measurements of the scattered electric field. It is often used for analysis purposes. For instance, to reduce the interference of wind turbine blades with air traffic control radars [1], to characterize tree signatures for canopy monitoring [2] or to identify and characterize radar reflectivity components of complex objects with the aim of reducing them [3]. In this case it is called radar cross section analysis or "RCS analysis." The paper focus on analysis imaging of low-RCS (i.e., stealthy) objects. In this context, the data are usually collected nearby, e.g., inside an indoor facility, if the object is small enough, in order to mitigate spurious echoes. RCS analysis can be one-dimensional (1-D) or 2-D, leading, respectively, to 1-D backscattering profiles or 2-D backscattering maps. 3-D radar images are known to be far more complicated and challenging to process [3]. Indeed, while a 2-D backscattering image can be formed by synthesizing a 1-D aperture with a wide-band radar, a 3-D backscattering image needs an entire 2-D aperture. Typical 2-D aperture geometries are planar, spherical, or cylindrical [4]. Once the backscatter field data are recorded, they are processed for radar image formation, i.e., to get 3-D images of the target radar backscattering spatial distribution.

Many techniques have been developed for 3-D radar image formation, specially in synthetic aperture radar (SAR) where the radar platform is moving while the target stays motionless, and ISAR (Inverse SAR), where the target is moving while the radar platform radar is immobile, is generally preferred for indoor RCS analysis. High resolution (HR) radar images are obtained by coherently processing the backscattered fields as a function of the frequency and the angle (i.e., object attitude relatively to the radar). Among the 3-D HR radar imaging techniques emphasized in [4], there is the polar format algorithm (PFA) [5], also known as Range-Doppler, the range migration algorithm (RMA), its 2-D version also being known as ω-k algorithm, and the chirp scaling algorithm. Based on the polar nature of the frequency-domain backscatter data, 3-D PFA is extensively used [6]. Taking advantage of the processing that in far-field condition is reduced to a Fourier synthesis problem, it is practically achieved via an interpolation that reformats the data in the spatial frequency domain, and an inverse fast Fourier transform (FFT). Refer to [3] or [7] for implementation details on 3-D PFA, including the polar reformatting mapping technique. Regarding the RMA, it comes from seismic engineering and geophysics. Based on 1-D Stolt interpolation and, again, FFT through an approximation with the method of stationary phase (MSP), RMA is able to compensate for a potential wavefront curvature completely. The last one, i.e., the chirp scaling algorithm, is widely used in airborne SAR. We will also mention space-time domain methods, such as the 3-D Backprojection (BP) algorithm. Also known as time-domain correlation, this tomographic reconstruction [5] is achieved by coherent sum-

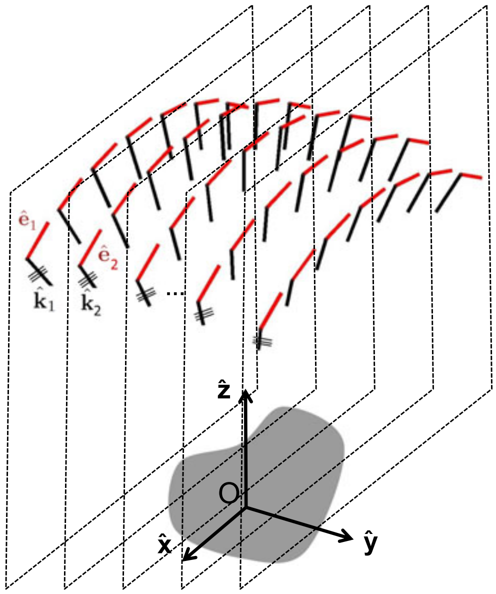

Fig. 1. 3-D RCS measurement facility (left), imaging geometry used in the measurement: side view (a) and (b) top view.

mation and stems from the projection-slice theorem; see for example [8]. Let us also mention the 3-D radar imaging techniques for wide aperture [9], ISAR [10], [11], or 3-D interferometric SAR [12] that provides stereoscopic vision from radar images of the same area. More specifically, [13] proposes to extract scatterers and, based on geometrical theory of diffraction, to identify them.

Nevertheless, despite these techniques, 3-D radar imaging for low-RCS analysis is still a real challenge. Every weak reflectivity component participating in the global RCS of the target under test must be identified and characterized at various wave frequencies, illumination angles, and polarizations. In fact, the physical implementations of the above-mentioned 2-D aperture geometries necessitate numerous illumination viewpoints around the object. It is a time-consuming task that involves many successive object and/or antenna rotations and stabilizations, with an accurate positioning system and repeatability capacity. As a consequence, the measurement time is rather long, with drift. This is specially tricky for low-RCS analysis. Indeed, the instrumentation and the environment must be all the more stable as the target RCS is low. If they are not stable enough, the vector subtraction step that is supposed to reduce the spurious echoes, caused by noise and environment coupling, has to be more efficient. To deal with these low-RCS analysis issues, the indoor spherical experimental setup of Fig. 1 has been developed [14]–[16]. Related to other 3-D spherical RCS setups [17], [18], it is composed of a 4-m radius motorized rotating arch (horizontal axis) that holds the measurement antennas while the target is located on a mast mounted on a rotating positioning system (vertical axis). Here, the imaging geometry differs notably from the usual ones (see for example [2]): the emitting/receiving antenna is roughly above the target under test, with a *complete* target rotation around the vertical axis, determined by the roll angle $\varphi \in [0^\circ, 360^\circ]$ and a limited arch rotation around the horizontal axis, determined by the azimuth angle $\theta \in [0^\circ, 20^\circ]$). This imaging geometry is particularly appropriate to the needs of low-RCS analysis. The residual echo signal or background signal can be more efficiently reduced in the useful zone. This reduction is achieved by high measurement performances [14], after various optimizations (robust mechanical design, position control system, arch design, lens-equipped horn, etc.). Since the target under test is located vertically below the antenna, materials like polystyrene can be considered to support the object [15], [16]; they are placed on the roll motor. All these efforts lead to high-quality positioning repeatability of the measurement antenna (the angular positioning repeatability of less than $1/1000^\circ$) and very efficient background signal subtraction. Although the imaging geometry of Fig. 1 is adapted to low-RCS analysis, it involves specific measurements that differ from standard ones [2]. The electric field direction is no longer constant relatively to the target under test. Due to the successive θ and φ rotations, its trajectory is concentric, forming successive growing circles with a singularity in the vertical direction. Conventional imaging methods, such as 3-D PFA [4], cannot be directly applied to process such collected data. An original approach, briefly introduced in [19], is developed and detailed in the current paper. It is shown that it leads to an inverse problem that can be solved by a fast regularization algorithm incorporating 3-D PFA. It determines three huge 3-D scatterer maps at once, corresponding to different polarizations at emission and reception [19]. Thus, the maps are computed from a single pass collection, whereas traditional algorithms unsuited to these concentric measurements would require two passes.

The paper is organized as follows. First, in Section II, a general description of the problem is provided. The following Section III is dedicated to the 3-D radar imaging approach. From the standard multiple scatterer (MS) model, a direct model is expressed for the concentric-varying electric field imaging geometry. This leads to the proposition of a fast regularized inversion method. In Section IV, after a few details on the instrumentation and process measurement, results are presented and discussed for various mock-ups, with comparisons to conventional 3-D PFA. Finally, the conclusions are summarized in Section V.

II. PROBLEM FORMULATION

After a brief introduction to standard RCS analysis, based on 3-D radar imaging, the problem of imaging from concentric collected data is described, with the expression of a more generic problem.

A. Standard RCS Analysis

In standard RCS analysis, a monostatic radar illuminates an object with a quasi-planar monochromatic continuous wave (CW) of given frequency f. The incident electric field is vector $\mathbf{E}^I$ of complex amplitude E^I. The object backscatters a CW with the same frequency. The

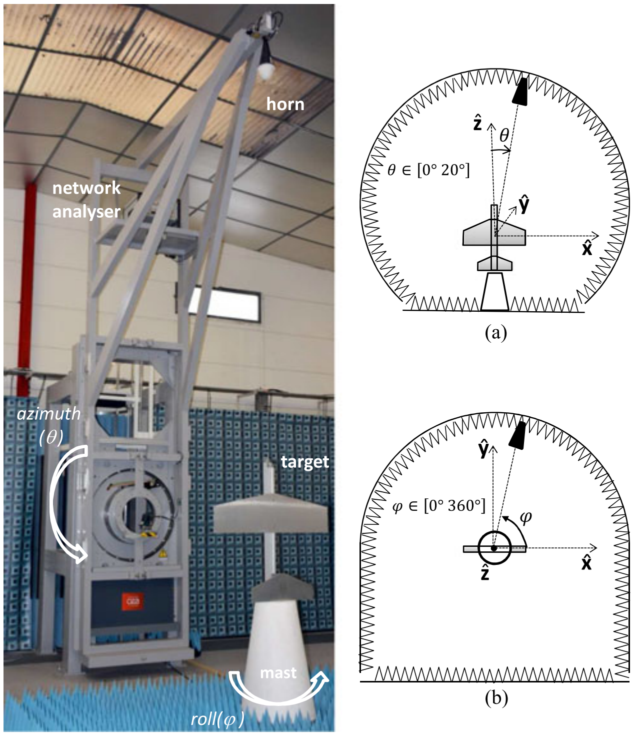

Fig. 2. Classical spherical radar imaging collection with quasi-constant electric field: the object (below) is illuminated by a sequence of EM waves whose wave vector (black) and electric field (red) directionsare coplanar.

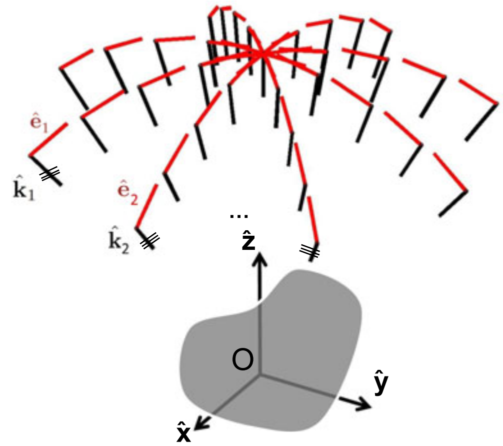

Fig. 3. Concentric radar imaging collection: the object (below) is illuminated by a sequence of EM waves with associated wave vector (black) and electric field (red) directions.

scattered electric field is vector $\mathbf{E}^S$, of complex amplitude E^S. The complex scattering coefficient $\mathcal{S}$ quantifies the whole object-EM wave interaction, with both wave change in amplitude and phase. Note that it is directly linked to the RCS. They can be defined in far field condition by (see [20] for more details):

$$\mathcal{S} = \lim_{R\to\infty} 2\sqrt{\pi} R \frac{\mathrm{E}^S}{\mathrm{E}^I}, \quad \mathrm{RCS} = |\mathcal{S}|^2 \tag{1}$$

where R is the radar distance at which scattering is observed. The complex scattering coefficient $\mathcal{S}$ can be measured with an appropriate instrumentation system (antenna, network analyzers, etc.) and a calibration process. The measurements can be repeated for different wave frequencies; this is usually called "stepped frequency continuous wave" acquisition mode. They can also be repeated for different incidence angles, by rotating the object and/or the antenna. Finally, the data are made of a sequence of M measured complex scattering coefficients $\{\mathcal{S}_1, \mathcal{S}_2, \ldots, \mathcal{S}_M\}$. Considering all these successive measurements, it is generally assumed in HR radar imaging that the wave-object interaction nature is unaltered. In particular, the polarization configuration remains stable, i.e., the electric field orientation relative to the target is unchanged. This is illustrated in Fig. 2 (where the azimuth rotation is exaggerated for the purposes of understanding).

For a given radar viewpoint (e.g., $O\hat{\mathbf{z}}$), radar imaging processing consists of the determination of the complex 3-D image or map $\mathcal{I}$, i.e., the complex amplitudes s_i at spatial grid points $\mathbf{r}_i$. It is an inverse problem, commonly based on the so-called multiple scattered model, where the target is considered as a collection of coherent illuminated and localized point scatterers. A "small bandwidth small angle" condition is usually assumed. It should be pointed out that it requires the electric field direction, i.e., the polarization vector, to remain constant so that the target-wave interaction does not vary from one measurement to another. The PFA, introduced above, is standard for 3-D ISAR. The computation of $\mathcal{I}$ is achieved via the inverse Fourier transform of the measured hologram, $\mathcal{S}_j$ (for $j = 1, \ldots, M$). In practice, the limited and discrete acquisition in angles and in frequencies must be taken into account. Furthermore, for a regular acquisition in angle and frequency, an interpolating preprocessing step of regridding is performed before an inverse 3-D FFT.

B. Low-RCS Analysis

Back to the experimental layout of Fig. 1, dedicated to low-RCS analysis. The goal is to analyze the scattering (from $O\hat{\mathbf{z}}$ viewpoint) from the concentric measurements of Fig. 3. In this singular setup, each measurement is associated with a different linear polarization, i.e., a different electric field direction. Let us focus on the ith measurement at wave frequency f_i. It is described by the wave vector $\mathbf{k}_i$, i.e., its direction (unit vector $\hat{\mathbf{k}}_i$) and its modulus or frequency wavenumber $\mathrm{k}_i = 2\pi f_i/c$ (where c denotes the light speed), by the polarization vector at emission (unit Jones vector $\hat{\mathbf{e}}_i^E$) and by the polarization vector at reception (unit Jones vector $\hat{\mathbf{e}}_i^R$). The incident electric field $\mathbf{E}_i^I$ is collinear to $\hat{\mathbf{e}}_i^E$ while $\hat{\mathbf{k}}_i \wedge \hat{\mathbf{e}}_i^E$ indicates the direction of the incident magnetic field. Finally, the measurement is defined, i.e., both microwave emission and reception, by the successive frequencies $\{f_1, f_2, \ldots, f_M\}$ and the successive corresponding directional triplets $\{(\hat{\mathbf{k}}_1, \hat{\mathbf{e}}_1^E, \hat{\mathbf{e}}_1^R), (\hat{\mathbf{k}}_2, \hat{\mathbf{e}}_2^E, \hat{\mathbf{e}}_2^R), \ldots, (\hat{\mathbf{k}}_M, \hat{\mathbf{e}}_M^E, \hat{\mathbf{e}}_M^R)\}$.

More generally, the 3-D radar imaging problem addressed consists in determining 3-D scatterer maps (from

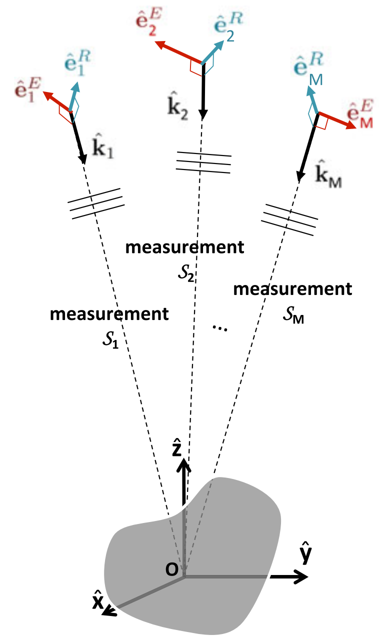

Fig. 4. Concentric radar imaging acquisition: the object (below) is illuminated by a sequence of EM waves with frequencies $\{f_1, f_2, \ldots, f_M\}$ and with associated wave vector (black) and electric field (red) directions.

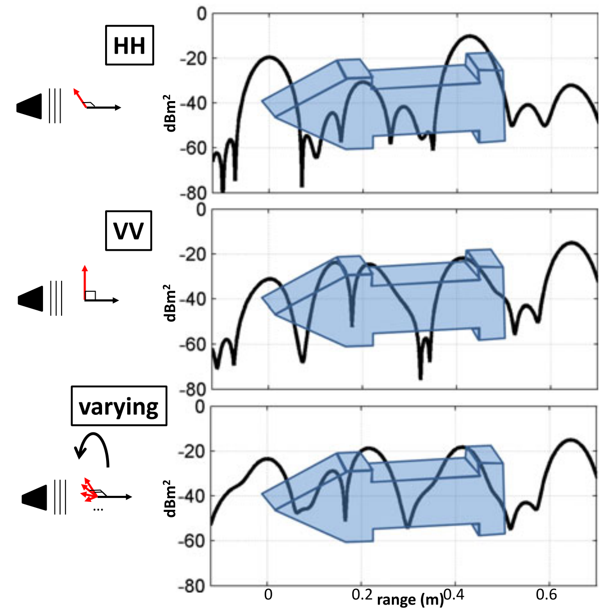

Fig. 5. Conventional HRR imaging and varying polarization of an arrow, from HH measurements (above), VV measurements (middle), and varying polarization measurements (below).

$O\hat{\mathbf{z}}$ radar viewpoint) based on this sequence of measurements with a varying electric field direction. See the generic representation in Fig. 4. Compared to classical radar imaging, the main issue is linked with the variation of polarization, i.e., the rotation of both the electric and magnetic fields. Indeed, the classical multiple isotropic scatterer model on which radar imaging usually relies cannot be used directly. Whereas the backscatter data are usually recorded separately for each polarization at emission and reception (i.e., HH, VV, and HV) in classical radar imaging, here all the information is "mixed-up." Additionally, it must be stressed that for this high dimensional problem the huge number of unknown quantities needs to be processed efficiently. The varying polarization issue is illustrated in Fig. 5. It corresponds to basic high resolution range (HRR) imaging, based on FFT, of a metallic arrow. From a frequency sweep at polarization HH or VV, an associated profile can be computed, providing information about the main scatterers. When the polarization varies, here at each frequency of the sweep, the resulting profile is a mixture that differs from the previous ones. In this condition, RCS analysis turns out to be tricky since it is not possible to extract or guess HH and VV information from it.

III. FAST 3-D RADAR IMAGING WITH CONCENTRIC MEASUREMENTS

Let us briefly introduce classical HR radar imaging [3] and first the ubiquitous "MS" model on which it is based. The MS model relies on the interpretation of the target-electromagnetic wave interaction by a collection of coherent illuminated and localized point scatterers [21]. Related to the high frequency behavior of EM scattering from geometrically complex bodies, the MS model can be derived from Maxwell's equations by high frequency approximations [21]. It must be stressed that it requires several restrictive conditions and does not explicitly account for various EM phenomena: multiple scattering, creeping waves, etc. Even so, the MS model is practically and intensively used in radar interpretation and analysis, far beyond the validity of its assumptions. It works pretty well in the far field but necessitates a critical look at its output: possible artifacts may occur [21], mainly related to the above-mentioned EM phenomena.

In a monostatic radar context with far field/planar monochromatic wave (with wave vector $\mathbf{k}_i$), the MS model considers a target made of N elementary isotropic scatterers. They are located at points $\mathbf{r}_n$ ($n = 1, \ldots, N$), of coordinates (x_n, y_n, z_n) in the target coordinate system $(O\hat{\mathbf{x}}\hat{\mathbf{y}}\hat{\mathbf{z}})$. Each scatterer is defined by its complex scattering coefficient or power s_n ($n = 1, \ldots, N$), which quantifies the relationship between the incident and scattered field amplitudes (E^I and E_n^S)[1], resulting from the elementary wave-scatterer interaction. In the MS model, the received echo or scattered signal is ideally formulated as a coherent superposition of elementary echoes [21], neglecting multiple scattering terms. That leads to the following MS model:

$$\mathcal{S}_i = \sum_{n=1}^{N} s_n \cdot e^{-2j\mathbf{k}_i \cdot \mathbf{r}_n}. \tag{2}$$

The N complex scattering coefficients s_n associated with the multiple scatterers determine the system response. They do not depend on the wave vector $\mathbf{k}_i$, i.e., its

[1]It is assumed that the incident scattered field amplitude E^I does not depend on n.

amplitude and direction. Consider the typical acquisition of Fig. 2 that can be encountered in spherical 3-D radar imaging. It requires a sequence of M viewpoints around $O\hat{\mathbf{z}}$. It must be noted that in such an acquisition the electric field varies slightly as long as the view angle variations are limited. This is also called the "small angle" condition. Moreover, the electric field stays in the same plane, as shown in Fig. 2, and the polarization remains more or less constant. Another condition is required: this is the "small bandwidth" condition. It implies that the target-wave interaction does not vary significantly within the limited frequency variation domain. If these conditions are fulfilled, each complex scattering coefficient s_n is considered constant for all the measurements.

Finally, the MS model can be formulated as

$$\mathcal{S}_i = \int \mathcal{I}(\mathbf{r}) \cdot e^{-2j\mathbf{k}_i \cdot \mathbf{r}} \cdot d\mathbf{r} + \varepsilon_i \tag{3}$$

where $\mathcal{I}(\mathbf{r}) = \sum_{n=1}^{N} s_n \delta(\mathbf{r} - \mathbf{r}_n)$ is the spatial density of scatterers and $\delta(\cdot)$ is the Dirac function. The additive term ε_i accounts for noise and uncertainty, due to interfering echoes generated by the environment and MS model limitations. It is generally considered as white and Gaussian (centered, complex, and circular).

A. Direct Model

Considering the concentric acquisition of Fig. 4, the multiple scatter model is no longer valid and as a consequence conventional radar imaging processing cannot be applied. Indeed, the complex scattering coefficients s_n $(n = 1, \ldots, N)$ can no longer be considered as quasi-constant from one illumination angle to another. The electromagnetic interaction is known to strongly depend on the electric field direction; consider, for example, the scattering with the edges of an object. To overcome this issue, we next express the MS model in this context; it will later support the imaging inversion process. Remember that the purpose is to achieve a radar imaging analysis from the $O\hat{\mathbf{z}}$ radar viewpoint. Let us consider the ith acquisition of Fig. 4, around $O\hat{\mathbf{z}}$. Then, the basic idea is to consider that each elementary isotropic scatterer is described with not only a complex scattering coefficient s_n but with a full polarization scattering matrix $\mathbf{S}_n$:

$$\mathbf{S}_n = \begin{bmatrix} s_n^{\mathrm{xx}} & s_n^{\mathrm{xy}} \\ s_n^{\mathrm{xy}} & s_n^{\mathrm{yy}} \end{bmatrix}. \tag{4}$$

More precisely known as the *RCS matrix* [22], $\mathbf{S}_n$ is defined in the target reference frame $O\hat{\mathbf{x}}\hat{\mathbf{y}}$, associated with an illumination direction collinear to vector $\hat{\mathbf{z}}$. It quantifies the amplitude and polarization of the scattered wave for an arbitrary polarization of the incident wave. Note that $s_n^{\mathrm{xy}} = s_n^{\mathrm{yx}}$ due to the reciprocity theorem for a monostatic case [23], so that the scattering matrix $\mathbf{S}_n$ is completely defined by the three complex coefficients: s_n^{xx}, s_n^{yy}, and s_n^{xy}.

Close to polarimetric radar imaging [23], [24], it is then straightforward to derive the following extended MS model that incorporates noise:

$$\mathcal{S}_i = \sum_{n=1}^{N} s_n^{\star}(i) \cdot e^{-2j\mathbf{k}_i \cdot \mathbf{r}_n} + \varepsilon_i \tag{5}$$

with

$$s_n^{\star}(i) = [\hat{\mathbf{e}}_i^R \cdot \hat{\mathbf{x}}' \quad \hat{\mathbf{e}}_i^R \cdot \hat{\mathbf{y}}'] \cdot \mathbf{S}_n'(i) \cdot \begin{bmatrix} \hat{\mathbf{e}}_i^E \cdot \hat{\mathbf{x}}' \\ \hat{\mathbf{e}}_i^E \cdot \hat{\mathbf{y}}' \end{bmatrix} \tag{6}$$

where $\mathbf{S}_n'(i)$ is the scattering matrix in the reference frame $O\hat{\mathbf{x}}'\hat{\mathbf{y}}'$, normal to the current direction of propagation $\hat{\mathbf{k}}_i$. Note that there is no component of $\mathbf{E}_n^S$ and $\mathbf{E}_i^I$ in the direction of $\hat{\mathbf{k}}_i$. For each illumination and associated radar imaging geometry, (5) introduces the appropriate combination of scattering matrix terms. As previously with the MS model about the scattering coefficients s_n, a "small bandwidth small angle" is assumed about the scattering matrices. Due to a limited acquisition domain, in angle (around $O\hat{\mathbf{z}}$) and frequency, the scattering matrices are assumed to be quasi-constant: $\mathbf{S}_n'(i) \approx \mathbf{S}_n$ for $i = 1, \ldots, M$. The above expression (6) leads to

$$s_n^{\star}(i) \approx [\hat{\mathbf{e}}_i^R \cdot \hat{\mathbf{x}}' \quad \hat{\mathbf{e}}_i^R \cdot \hat{\mathbf{y}}'] \cdot \mathbf{S}_n \cdot \begin{bmatrix} \hat{\mathbf{e}}_i^E \cdot \hat{\mathbf{x}}' \\ \hat{\mathbf{e}}_i^E \cdot \hat{\mathbf{y}}' \end{bmatrix}. \tag{7}$$

Basically, this expression provides the complex scattering coefficients or powers $s_n^{\star}$ of the MS model that are adapted to the ith geometrical configuration. Note again that it depends on the relative target attitude toward the emitting and receiving antenna. In classical radar imaging, the directions of $\hat{\mathbf{e}}_i^E$ and $\hat{\mathbf{e}}_i^R$ remain stable, constantly selecting a term of the scattering matrix $\mathbf{S}_n$ or a fixed linear combination of them. In this varying electric field direction context, they are all "mixed": (5) and (7) show that each acquisition is to select a different combination of the scattering matrix $\mathbf{S}_n$. Next, the extended MS model is detailed for the specific setup of Fig. 1.

1) Specific Form for Concentric Measurements Let us consider the concentric acquisition, with the successive wave and electric field vectors represented in Fig. 3. It stems from a spherical 3-D RCS setup that will be further detailed in Section IV. First, note the following sort of singularity: the vectors spin around axis $\hat{\mathbf{z}}$ and there are various acquisitions from wave vectors colinear to $\hat{\mathbf{z}}$ while electric fields differ. Note that it induces different scattered fields; it goes against the classical MS model with scalars s_n.

The ith measurement is determined by $(\theta_i, \varphi_i, f_i)$, for $i = 1, \ldots, M$. The azimuth θ_i and the roll φ_i correspond to two rotation angles (the roll rotation is defined around $\hat{\mathbf{z}}$, see Section IV for details). This defines the directions of the wave vector direction $\hat{\mathbf{k}}_i$:

$$\hat{\mathbf{k}}_i = \begin{bmatrix} -\sin\theta_i \cos\varphi_i \\ -\sin\theta_i \sin\varphi_i \\ -\cos\theta_i \end{bmatrix}_{(\hat{\mathbf{x}}, \hat{\mathbf{y}}, \hat{\mathbf{z}})}$$

and the emitting/receiving linear polarization $\hat{\mathbf{e}}_i^E$:

$$\hat{\mathbf{e}}_i^E = \begin{bmatrix} -\cos\theta_i \cos\varphi_i \\ -\cos\theta_i \sin\varphi_i \\ \sin\theta_i \end{bmatrix}_{(\hat{\mathbf{x}},\hat{\mathbf{y}},\hat{\mathbf{z}})} \quad \text{or} \quad \begin{bmatrix} -\sin\varphi_i \\ \cos\varphi_i \\ 0 \end{bmatrix}_{(\hat{\mathbf{x}},\hat{\mathbf{y}},\hat{\mathbf{z}})}$$

depending on the emitting and receiving linear polarized mode of the antenna (respectively, H or V), and so for $\hat{\mathbf{e}}_i^R$.

Afterward, we determine the specific forms of $(\hat{\mathbf{e}}_i^R \cdot \hat{\mathbf{x}}', \hat{\mathbf{e}}_i^R \cdot \hat{\mathbf{y}}')$ and $(\hat{\mathbf{e}}_i^E \cdot \hat{\mathbf{x}}', \hat{\mathbf{e}}_i^E \cdot \hat{\mathbf{y}}')$ in order to express $s_n^\star(i)$ for concentric acquisition. First of all, let us define the intermediate coordinate system $(\hat{\mathbf{x}}_0', \hat{\mathbf{y}}_0', \hat{\mathbf{z}}_0')$:

$$\hat{\mathbf{z}}_0' = -\hat{\mathbf{k}}_i \tag{8}$$

$$\hat{\mathbf{y}}_0' = \frac{\hat{\mathbf{z}}_0' \wedge \hat{\mathbf{z}}}{\| \hat{\mathbf{z}}_0' \wedge \hat{\mathbf{z}} \|} = \begin{bmatrix} -\sin\varphi_i \\ \cos\varphi_i \\ 0 \end{bmatrix}_{(\hat{\mathbf{x}},\hat{\mathbf{y}},\hat{\mathbf{z}})} \tag{9}$$

$$\hat{\mathbf{x}}_0' = \hat{\mathbf{y}}_0' \wedge \hat{\mathbf{z}}_0' = \begin{bmatrix} \cos\theta_i \cos\varphi_i \\ \cos\theta_i \sin\varphi_i \\ -\sin\theta_i \end{bmatrix}_{(\hat{\mathbf{x}},\hat{\mathbf{y}},\hat{\mathbf{z}})}. \tag{10}$$

The unit Jones vector at emission $\hat{\mathbf{e}}_i^E$, and so at reception $\hat{\mathbf{e}}_i^R$, can be expressed in $(\hat{\mathbf{x}}_0', \hat{\mathbf{y}}_0')$ as: $\hat{\mathbf{e}}_i^E = [-1 \quad 0]^{\mathrm{t}}_{(\hat{\mathbf{x}}_0', \hat{\mathbf{y}}_0')}$ (H mode) or $[0 \quad 1]^{\mathrm{t}}_{(\hat{\mathbf{x}}_0', \hat{\mathbf{y}}_0')}$ (V mode). The antenna coordinate system $(\hat{\mathbf{x}}', \hat{\mathbf{y}}', \hat{\mathbf{z}}')$ is defined by: $\hat{\mathbf{z}}' = \hat{\mathbf{z}}_0' = -\hat{\mathbf{k}}_i$, $\hat{\mathbf{x}}'$ is collinear to the projection of $\hat{\mathbf{x}}$ on the orthogonal plane $(\hat{\mathbf{x}}_0', \hat{\mathbf{y}}_0')$ and $\hat{\mathbf{y}}' = \hat{\mathbf{z}}' \wedge \hat{\mathbf{x}}'$:

$$\hat{\mathbf{x}}' = \frac{\cos\theta_i \cos\varphi_i \hat{\mathbf{x}}_0' - \sin\varphi_i \hat{\mathbf{y}}_0'}{\sqrt{\cos^2\theta_i \cos^2\varphi_i + \sin^2\varphi_i}} \tag{11}$$

$$\hat{\mathbf{y}}' = \frac{\sin\varphi_i \hat{\mathbf{x}}_0' + \cos\theta_i \cos\varphi_i \hat{\mathbf{y}}_0'}{\sqrt{\cos^2\theta_i \cos^2\varphi_i + \sin^2\varphi_i}}. \tag{12}$$

For the H mode, it results in the following expressions for $\hat{\mathbf{e}}_i^E \cdot \hat{\mathbf{x}}'$ and $\hat{\mathbf{e}}_i^E \cdot \hat{\mathbf{y}}'$ (and so $\hat{\mathbf{e}}_i^R$):

$$\mathbf{e}^I \cdot \hat{\mathbf{x}}' = \frac{-\cos\theta_i \cos\varphi_i}{\sqrt{\cos^2\theta_i \cos^2\varphi_i + \sin^2\varphi_i}} \tag{13}$$

$$\mathbf{e}^I \cdot \hat{\mathbf{y}}' = \frac{-\sin\varphi_i}{\sqrt{\cos^2\theta_i \cos^2\varphi_i + \sin^2\varphi_i}}. \tag{14}$$

Let us sum up the complex scattering coefficient in this concentric acquisition. For the ith polarization acquisition, the complex coefficient $s_n^\star(i)$ is given by

(1) *HH acquisition mode*

$$\begin{aligned} s_n^\star(i) &\approx [\hat{\mathbf{e}}_i^R \cdot \hat{\mathbf{x}}' \quad \hat{\mathbf{e}}_i^R \cdot \hat{\mathbf{y}}'] \cdot \mathbf{S}_n \cdot \begin{bmatrix} \hat{\mathbf{e}}_i^E \cdot \hat{\mathbf{x}}' \\ \hat{\mathbf{e}}_i^E \cdot \hat{\mathbf{y}}' \end{bmatrix} \\ &\approx \frac{1}{\mathcal{K}_i}[\cos^2\theta_i \cos^2\varphi_i \cdot s_n^{\mathrm{xx}} + \sin^2\varphi_i \cdot s_n^{\mathrm{yy}} \\ &\quad + \cos\theta_i \sin 2\varphi_i \cdot s_n^{\mathrm{xy}}]. \end{aligned} \tag{15}$$

(2) *VV acquisition mode*

$$\begin{aligned} s_n^\star(i) \approx \frac{1}{\mathcal{K}_i}&[\sin^2\varphi_i \cdot s_n^{\mathrm{xx}} + \cos^2\theta_i \cos^2\varphi_i \cdot s_n^{\mathrm{yy}} \\ &- \cos\theta_i \sin 2\varphi_i \cdot s_n^{\mathrm{xy}}]. \end{aligned} \tag{16}$$

(3) *HV acquisition mode*

$$\begin{aligned} s_n^\star(i) \approx \frac{1}{\mathcal{K}_i}\Bigg[&\cos\theta_i \frac{\sin 2\varphi_i}{2} \cdot s_n^{\mathrm{xx}} - \cos\theta_i \frac{\sin 2\varphi_i}{2} \cdot s_n^{\mathrm{yy}} \\ &-(\cos^2\theta_i \cos^2\varphi_i - \sin^2\varphi_i) \cdot s_n^{\mathrm{xy}}\Bigg] \end{aligned} \tag{17}$$

with: $\mathcal{K}_i = \cos^2\theta_i \cos^2\varphi_i + \sin^2\varphi_i$.

Let us consider all the measurements, i.e., the M observed complex scattering coefficients, in the associated acquisition conditions defined by the successive frequencies f_i, azimuth θ_i and roll φ_i for $i \in 1, \ldots, M$. They are stacked in the following complex vector $\boldsymbol{\mathcal{S}}$:

$$\boldsymbol{\mathcal{S}} = [\mathcal{S}_1 \quad \mathcal{S}_2 \quad \cdots \quad \mathcal{S}_M]^{\mathrm{t}}. \tag{18}$$

2) *Derived Direct Matrix Model:* Now, the observation model (forward model) is derived from the previous extended MS model. Let us stress again that the "small bandwidth small angle" is assumed: the scattering matrices are supposed to be nearly constant in the limited acquisition domain. The unknown is made up of the scattering matrices associated with the N discretized scatter points $\mathbf{r}_n$ $(n = 1, \ldots, N)$ of a 3-D grid, the coordinates of which are (x_n, y_n, z_n) in the target coordinate system $(O\hat{\mathbf{x}}\hat{\mathbf{y}}\hat{\mathbf{z}})$. The scattering matrices can be separated in three 3-D maps $\boldsymbol{s}_{\mathrm{xx}}$, $\boldsymbol{s}_{\mathrm{yy}}$ et $\boldsymbol{s}_{\mathrm{xy}}$ (in the target reference frame), respectively for HH, VV, and HV antenna polarization mode (defined at the initial reference rotation, for $\theta = 0^\circ$ and $\varphi = 0^\circ$). In vector form, they can be expressed, respectively, by: $\boldsymbol{s}_{\mathrm{xx}} = \left[s_1^{\mathrm{xx}} \quad s_2^{\mathrm{xx}} \quad \cdots \quad s_N^{\mathrm{xx}}\right]^{\mathrm{t}}$, $\boldsymbol{s}_{\mathrm{yy}} = \left[s_1^{\mathrm{yy}} \quad s_2^{\mathrm{yy}} \quad \cdots \quad s_N^{\mathrm{yy}}\right]^{\mathrm{t}}$, and $\boldsymbol{s}_{\mathrm{xy}} = \left[s_1^{\mathrm{xy}} \quad s_2^{\mathrm{xy}} \quad \cdots \quad s_N^{\mathrm{xy}}\right]^{\mathrm{t}}$. From (5), the complex scattering coefficients $\mathcal{S}_i$ are clearly related to the Fourier transform of the $s_n^\star$ coefficients. Furthermore, it is obvious from (15) and (16) that the scattering coefficients are linear combinations of components $\boldsymbol{s}_k$ $(k \in \{\mathrm{xx}, \mathrm{yy}, \mathrm{xy}\})$. Therefore, the direct model (5) can be rewritten as (with noise vector $\boldsymbol{\varepsilon}$):

$$\boldsymbol{\mathcal{S}} = \sum_{k \in \{xx, yy, xy\}} \boldsymbol{T}\boldsymbol{W}_k \boldsymbol{F}\boldsymbol{s}_k + \boldsymbol{\varepsilon} \tag{19}$$

where $\boldsymbol{F}$ is a discrete Fourier transform (DFT) that can be computed by FFT algorithm. Finally, $\boldsymbol{T}$ is the truncation matrix related to the position of the observed points in the Fourier domain. The three matrices $\boldsymbol{W}_k$ are diagonal weight matrices that affect Fourier coefficients $(k \in \{\mathrm{xx}, \mathrm{yy}, \mathrm{xy}\})$:

$$\boldsymbol{W}_k = \mathbf{diag}(\mathrm{w}_k(1), \mathrm{w}_k(2), \ldots, \mathrm{w}_k(M)). \tag{20}$$

Depending on the polarization acquisition mode (HH, VV, or HV), the weights $\boldsymbol{W}_k$ are given, respectively, by (15), (16), and (17). They define the elements or combination of elements of the N MS scattering matrices (i.e., s_n^{xx}, s_n^{yy}, or s_n^{xy}, for $n = 1, \ldots, N$), which determine the scattering coefficient observation $\mathcal{S}_i$. When the acquisition mode is HH, the weights are given by (for $i = 1, \ldots, M$):

$$\begin{cases} \mathrm{w}_{\mathrm{xx}}(i) = \cos^2\theta_i \cos^2\varphi_i / \mathcal{K}_i \\ \mathrm{w}_{\mathrm{yy}}(i) = \sin^2\varphi_i / \mathcal{K}_i \\ \mathrm{w}_{\mathrm{xy}}(i) = \cos\theta_i \sin 2\varphi_i / \mathcal{K}_i \end{cases}. \tag{21}$$

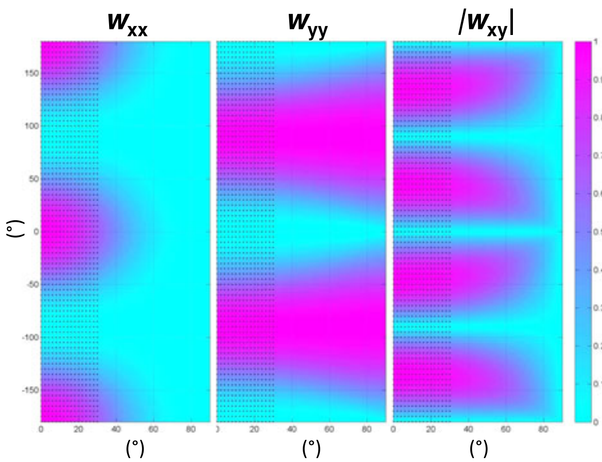

Fig. 6. Weigths $\mathrm{w_{xx}}$, $\mathrm{w_{yy}}$, and $|\mathrm{w_{xy}}|$ as a function of θ and φ, with typical acquisition angles (black points).

They are shown in Fig. 6, for various acquisition angles θ and φ. Typical acquisition angles, where $\theta \leq 30^\circ$ and $0^\circ \leq \varphi \leq 360^\circ$, are represented by black points. Note that the weights $\mathrm{w_{xx}}$, $\mathrm{w_{yy}}$, and $\mathrm{w_{xy}}$ depend mainly on the value of φ. As φ is close to 0°, only the s_n^{xx} terms matter. Conversely, when φ is close to $\pm 90^\circ$, only the s_n^{yy} matter and for that reason are observable. Note that this is true as long as $\theta \leq 40^\circ$. For larger θ, the scattering terms s_n^{xx} no longer affect the coherent superposition echo. At all events, the "small bandwidth small angle" assumption of constant $\mathbf{S}_n$ will be violated for common complex targets. In the end, to go back to the scattering coefficient observability depending on φ, the concentric collection pass provides information about all the scatterer maps but provides less information about a specific map, e.g., $\boldsymbol{s}_{\mathrm{xx}}$, than a conventional single pass dedicated to it.

Finally, merging the three maps in an unique column vector $\boldsymbol{s} = \left[\boldsymbol{s}_{\mathrm{xx}}; \boldsymbol{s}_{\mathrm{yy}}; \boldsymbol{s}_{\mathrm{xy}}\right]$, the final direct model reads

$$\boldsymbol{\mathcal{S}} = \boldsymbol{A}\boldsymbol{s} + \boldsymbol{\varepsilon} \tag{22}$$

where $\boldsymbol{A}$ is a large block matrix of size $M \times 3N$:

$$\boldsymbol{A} = \left[\, \boldsymbol{T}\boldsymbol{W}_{\mathrm{xx}}\boldsymbol{F} \middle| \boldsymbol{T}\boldsymbol{W}_{\mathrm{yy}}\boldsymbol{F} \middle| \boldsymbol{T}\boldsymbol{W}_{\mathrm{xy}}\boldsymbol{F} \,\right]. \tag{23}$$

The observation matrix $\boldsymbol{A}$ defines the deterministic part of the relation between the observations and the unknown state vector made of the three vectorized 3-D maps. It must be noted that its dimensions can be huge, e.g., $N \approx 500000$ and $M = 15 \cdot 10^6$. And yet, the model (22) is still linear (linear transforms and additive noise). Moreover, it relies on simple and fast transform (FFT, weight, truncation). Again, remark that a close parallel can be made with polarimetric SAR [23], [24].

B. Regularized Inversion

Regarding the inverse problem, a common approach relies on a discrepancy between measurements and model outputs. A standard discrepancy is based on a quadratic norm and yields the so-called least squares (LS) criterion:

$$\mathcal{J}_{\mathrm{LS}}(\boldsymbol{s}) = \|\boldsymbol{\mathcal{S}} - \boldsymbol{A}\boldsymbol{s}\|^2 . \tag{24}$$

A potential solution minimizes $\mathcal{J}_{\mathrm{LS}}$, i.e., it is the one that best fits the data:

$$\widehat{\boldsymbol{s}}_{\mathrm{LS}} = \underset{\boldsymbol{s}\in\mathbb{C}^N}{\arg\min}\, \mathcal{J}_{\mathrm{LS}}(\boldsymbol{s}). \tag{25}$$

The minimizer $\widehat{\boldsymbol{s}}_{\mathrm{LS}}$ can be found by setting the gradient of $\mathcal{J}_{\mathrm{LS}}(\boldsymbol{s})$ to zero and it leads to a linear system:

$$\boldsymbol{A}^\dagger\boldsymbol{A}\boldsymbol{s} = \boldsymbol{A}^\dagger\boldsymbol{\mathcal{S}}. \tag{26}$$

Unfortunately, it cannot be solved since $\boldsymbol{A}^\dagger\boldsymbol{A}$ is rank deficient (the number of unknowns is larger than the number of measurements) and, as a consequence, an infinity of objects minimizes (and nullifies) the LS criterion. In other words, an infinity of backscattered maps is exactly consistent with the data. Among these solutions, a possible simple approach selects the one with minimum norm:

$$\widehat{\boldsymbol{s}}_{\mathrm{MNLS}} = \begin{cases} \arg\min_{\boldsymbol{s}\in\mathbb{C}^N} \|\boldsymbol{s}\|^2 \\ \text{s.t. } \boldsymbol{\mathcal{S}} - \boldsymbol{A}\boldsymbol{s} = 0 \end{cases} \tag{27}$$

i.e., the minimum norm least squares (MNLS) solution. It can be viewed as the "less energetic solution" that is coherent with the data. In a way, it is known to be the less "compromising" solution since it puts to zero the coefficients of the solution associated to the eigenvectors of the observation operator that are linked with unobserved directions. The MNLS solution is robust as it reduces the possible impact of noise by preventing its propagation through unobserved components. There is a very abundant literature on various methods to deal with this kind of situations and build other solutions. The interested reader can, for instance, refer to books on inverse problems [25]–[29]. Coming back to our simple MNLS solution, it can be shown that

$$\widehat{\boldsymbol{s}}_{\mathrm{MNLS}} = \boldsymbol{A}^\dagger(\boldsymbol{A}\boldsymbol{A}^\dagger)^{-1}\boldsymbol{\mathcal{S}}\,. \tag{28}$$

A possible proof is based on Lagrange multipliers and it is given in Appendix A.

The estimated map $\widehat{\boldsymbol{s}}_{\mathrm{MNLS}}$ is a linear transform of the data, nevertheless the matrix $\boldsymbol{A}\boldsymbol{A}^\dagger$ is huge and its inverse cannot be computed. Fortunately, it can be inverted analytically: given the specificity of (23), we have

$$\boldsymbol{A}\boldsymbol{A}^\dagger = \boldsymbol{T}\,(\boldsymbol{W}_{\mathrm{xx}}^2 + \boldsymbol{W}_{\mathrm{yy}}^2 + \boldsymbol{W}_{\mathrm{xy}}^2)\,\boldsymbol{T}^{\mathrm{t}}$$

that is a diagonal matrix and hence easily invertible. Finally, relation (28) becomes

$$\widehat{\boldsymbol{s}}_{\mathrm{MNLS}} = \begin{bmatrix} \boldsymbol{F}^\dagger\boldsymbol{W}_{\mathrm{xx}}\boldsymbol{T}^{\mathrm{t}} \\ \boldsymbol{F}^\dagger\boldsymbol{W}_{\mathrm{yy}}\boldsymbol{T}^{\mathrm{t}} \\ \boldsymbol{F}^\dagger\boldsymbol{W}_{\mathrm{xy}}\boldsymbol{T}^{\mathrm{t}} \end{bmatrix} \left[\boldsymbol{T}\,(\boldsymbol{W}_{\mathrm{xx}}^2 + \boldsymbol{W}_{\mathrm{yy}}^2 + \boldsymbol{W}_{\mathrm{xy}}^2)\,\boldsymbol{T}^{\mathrm{t}}\right]^{-1}\boldsymbol{\mathcal{S}}$$

that jointly determines the three 3-D backscattered maps associated with the xx, yy, and xy polarizations. In addition, each individual map $\widehat{\boldsymbol{s}}_{\mathrm{MNLS}}^k$ is obtained separately by

$$\widehat{\boldsymbol{s}}_{\mathrm{MNLS}}^k = \boldsymbol{F}^\dagger\boldsymbol{W}_k\boldsymbol{T}^{\mathrm{t}}\left[\boldsymbol{T}\,(\boldsymbol{W}_{\mathrm{xx}}^2 + \boldsymbol{W}_{\mathrm{yy}}^2 + \boldsymbol{W}_{\mathrm{xy}}^2)\,\boldsymbol{T}^{\mathrm{t}}\right]^{-1}\boldsymbol{\mathcal{S}}$$

from the data-set $\boldsymbol{\mathcal{S}}$. It can be seen that they are obtained by IFFT of the zero-padded weighted measurements. The involved weights are:

$$\pi_k(m) = \frac{w_k(m)}{w_{\mathrm{xx}}(m)^2 + w_{\mathrm{yy}}(m)^2 + w_{\mathrm{xy}}(m)^2} \tag{29}$$

based on direct weight (21), which depends on the polarization mode and the acquisition angles (azimuth and roll). The resulting fast 3-D radar imaging algorithm is composed of two steps. The first step consists in processing the data by applying the weights of (29), for each polarization xx, yy, and xy, and for each associated weight. Afterward, in the second step, three 3-D backscattered maps, associated with xx, yy, and xy (in the target reference frame), are separately reconstructed by a 3-D PFA method [21], [30], that includes regridding and inverse 3-D IFFT steps. Interestingly, it is shown in Appendix B that the 3-D PFA component can also be derived as the MNLS solution in a classical acquisition geometry context. It is finally a very efficient implementation, based on weight, zero-padding, and IFFT.

Remark: For a classical acquisition geometry, i.e., quasi-constant electric field direction, our approach amounts to 3-D PFA. But for varying electric field direction, such as in the concentric data acquisition of the low-RCS analysis system, it will be shown further in Section IV that the direct application of 3-D PFA is inappropriate.

IV. APPLICATION

A. Instrumentation and Measurement Process

Let us give a few details about the instrumentation of the spherical setup (see Fig. 1). The microwave instrumentation is made up of two bipolarization monostatic radio frequency (RF) transmitting and receiving antennas that are driven by a fast network analyzer. A phased array antenna is used for the 0.8–1.8 GHz frequency band. It is optimized in order to reduce spurious signals originating from interactions with the arch metallic structure. For higher frequencies from 2 to 12 GHz, a wideband standard gain horn, equipped with a lens, is often preferred (see Fig. 1). If necessary, this illumination system is replaced by a phased array antenna, optimized specifically for a given frequency band. In X-band, a phased array antenna has been designed: it is optimized in order to reduce spurious signals that come to and from the arch metallic structure. Besides, as the cross polarization level is no more than -45 dB, the cross polarization errors can be neglected.

The arch is built of aluminum, weighs about 200 kg, measures approximately 5 m $\times$ 3 m, and is designed to minimize potential mechanical deformations and to hold the measurement antenna over a total travel range of $\pm 100^{\mathrm{o}}$. The θ rotation is achieved using a direct drive positioner including a brushless motor with a high accuracy encoder directly coupled to the motor for accuracy and repeatability concerns. The φ rotation uses another positioner also including a brushless motor with a high accuracy encoder directly coupled to the motor. The polystyrene mast [15], [16] supporting the target under test is located on this rotating positioning system (vertical axis). Let us emphasize the precision of the whole positioning system. The two major errors are the residual radial error and the repositioning (repeatability) error of the arch. The first one is about $\pm 0.001^{\mathrm{o}}$ and is equivalent to a maximum error of ± 0.75 mm on the vertical axis. The second one is about ± 0.15 mm maximum, once again on the vertical axis. Refer to [14] for details on the laser tracker characterization.

An important point for RCS measurement system is its dynamic range [22]. It is the ratio of the maximum to minimum usable target signal power and is linked with its sensitivity. The RF instrumentation of the spherical setup is designed to obtain a minimum of 120 dB of dynamic range. In this case, a signal-to-noise ratio of 20–30 dB corresponds to the minimum useful signal; it limits noise effects on the calibration accuracy. Note that the dynamic range can differ at various points of the receiver or the data acquisition system. Drift can reduce the dynamic range, especially in 3-D radar imaging where the collection pass is long. This time consuming task increases the potential instability of frequency, gain, and target position as well as instrumentation antennas and structure of the test range. All these several key issues have been considered during the design of this experimental layout [14] by minimizations of RF cable length, robust mechanical design, including a motor with a high accuracy encoder, temperature stabilization, etc. Moreover, modern RCS measurement transceivers, by their circuits and postprocessing techniques, contribute to reduce drift during the data acquisition. Consequently, no rotation stage has been positioned at the rear of the measurement antenna to modify the polarization wave. Indeed, it would have generated too much phase instability (due to movement of RF cables, rotary joint, etc.) and would have significantly increased the measurement time.

Concerning the measurement process, it is composed of successive stages. First, a calibration by substitution [22] is performed: this consists in replacing the test target with a calibration standard whose echo is well known in order to determine the inverse transfer function $\mathcal{K}$ of the entire RCS measurement system. This serves to indirectly convert the received transmitted electric field T_{out} to a complex scattering coefficient value: $\mathcal{S} = \mathcal{K}.T_{\mathrm{out}}$. Basically, the substitution method establishes a phase reference relatively to the rotation center and normalizes out the dispersive frequency response of the RCS measurement system. Note that for large objects, it can be enhanced by a multicalibration approach [31] which overcomes most near-field effects, such as the power decrease or the EM wave sphericity. The second stage corresponds to background subtraction [22]. It is commonly introduced when the clutter is too high, compared to the test target and calibration signals. It coherently removes the background echoes. Where necessary, an adaptive range filter is applied to eliminate the residual interferences, e.g., interactions with walls and floor that can affect the useful signal.

B. Results

Let us first illustrate our 3-D radar imaging method by an application to the following synthetic RCS data.

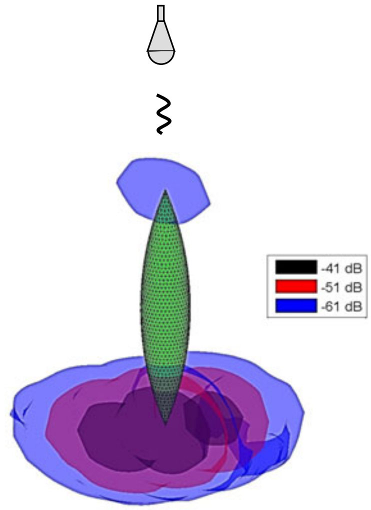

Fig. 7. Ogival shape 3-D radar map $\widehat{\boldsymbol{s}}^{\mathrm{xx}}_{\mathrm{MNLS}}$ $[N = 64 \times 64 \times 1024, M \approx 2 \cdot 10^5]$.

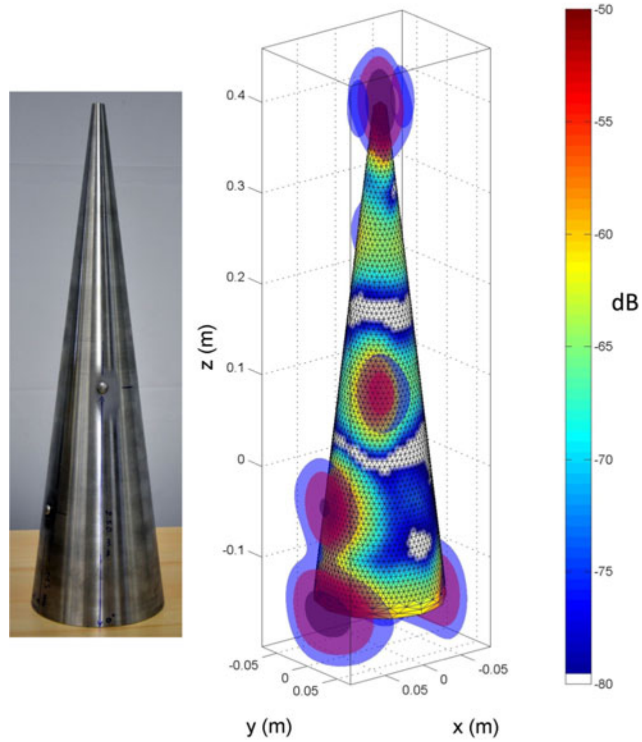

Fig. 8. Metallic cone with three metallic patches (left)—3-D radar map $\widehat{\boldsymbol{s}}^{\mathrm{xx}}_{\mathrm{MNLS}}$ $[N = 256 \times 256 \times 512, M \approx 10^5]$ (right).

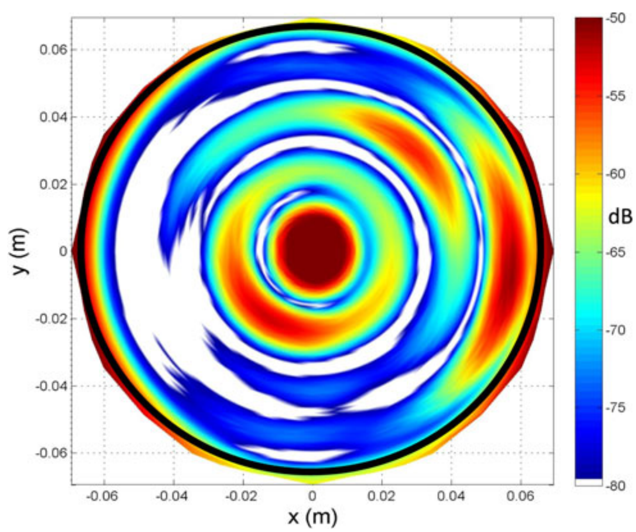

Fig. 9. Above view of the 3-D radar map $\widehat{\boldsymbol{s}}^{\mathrm{xx}}_{\mathrm{MNLS}}$ (shape section) $[N = 256 \times 256 \times 512, M \approx 10^5]$.

We consider the metallic ogival-shaped object from the EM benchmark [32], with concentric measurements at $\theta \in [0^\circ : 2^\circ : 20^\circ]$, $\varphi \in [0^\circ : 5^\circ : 360^\circ[$, and $f \in [1\ \mathrm{GHz} : 10\ \mathrm{MHz} : 3\ \mathrm{GHz}]$. The synthetic data are computed by an efficient parallelized harmonic Maxwell solver.[2] Fig. 7 shows the 3-D scatterer map $\widehat{\boldsymbol{s}}^{\mathrm{xx}}_{\mathrm{MNLS}}$, corresponding to xx polarization. The 3-D map corresponds to the indicated above radar viewpoint, along $O\hat{\mathbf{z}}$. Here, the 3-D volume is represented by several transparent isosurfaces that are linked to different scatterer levels. In this basic situation, the main EM scatterers are located: the diffraction on the above tip and, at a higher level, the diffraction on the below tip. It comes with side lobes that derive from the limited acquisition sampling.

Next, it is shown how the 3-D radar imaging approach can support RCS analysis in more complex situations from real concentric single pass measurement data. Various targets have been characterized in order to evaluate the 3-D radar imaging method: a metallic cone with patches and the metallic arrow of the HRR imaging illustration of Fig. 5. Each of them serves to test the capacity to deal with various target-wave interaction phenomena: localized scatterers with the metallic cone, multiple diffractions as well as different polarization responses with the metallic arrow. All the scattering measurements have been acquired for a 360° roll sweep (φ) and a $\pm 20^\circ$ azimuth sweep (θ), from 8.2 to 12.4 GHz frequency.

1) *Localized Scatterers:* Fig. 8 shows the 3-D radar map $\widehat{\boldsymbol{s}}^{\mathrm{xx}}_{\mathrm{MNLS}}$ in polarization xx of a metallic cone (height: 55 cm) where three metallic patches have been glued to points $z = 250$ mm (-45° roll), $z = 400$ mm (135° roll), and $z = 112$ mm (270° roll). For convenience, the 3-D volume is represented by several isosurfaces, superimposed upon a volume section relatively to the target shape. Notice that in the current and next figures, the target shape is used for better RCS analysis understanding, without any target recognition purpose, and not at all in the inversion process. The main scatterers are perfectly located: the tip, the diffraction of the rear edge, and each metallic patch. Note that since the frequency band is here larger than for the previous ogival-shaped object, the resolution is improved along $O\hat{\mathbf{z}}$. The scatterers corresponding to the three metallic patches are correctly located. This is confirmed in the above view of Fig. 9, where the image can be compared to the photo of Fig. 10, as well as in the exploded image

[2] It combines a volume finite element method and integral equation technique, taking benefit from the axisymmetrical geometry of the shape [33].

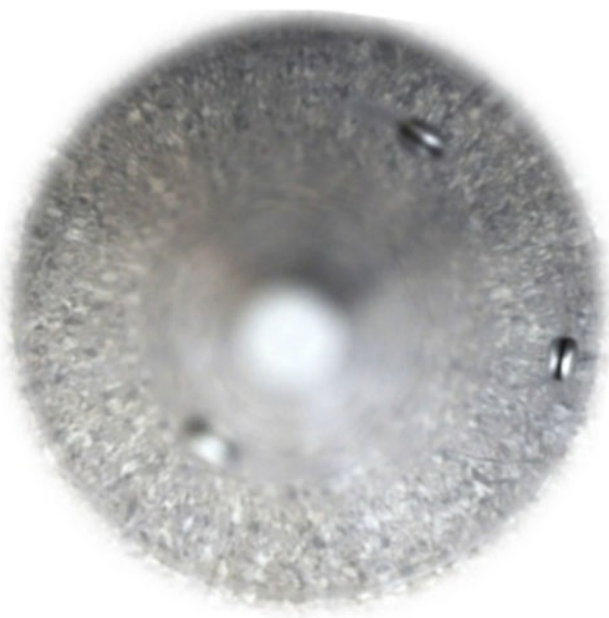

Fig. 10. Above view of the metallic cone with three metallic patches.

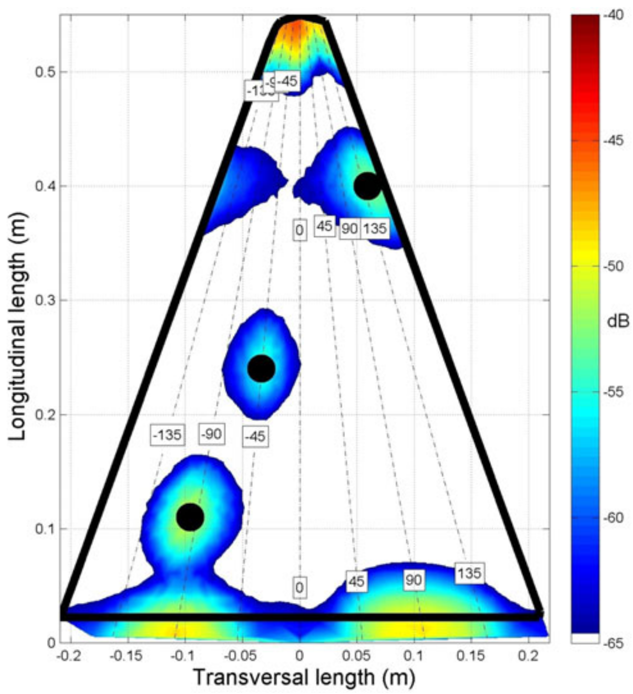

Fig. 11. Exploded image of the 3-D radar map $\widehat{\mathbf{s}}^{\mathrm{xx}}_{\mathrm{MNLS}}$
$[N = 256 \times 256 \times 512,\ M \approx 10^5]$.

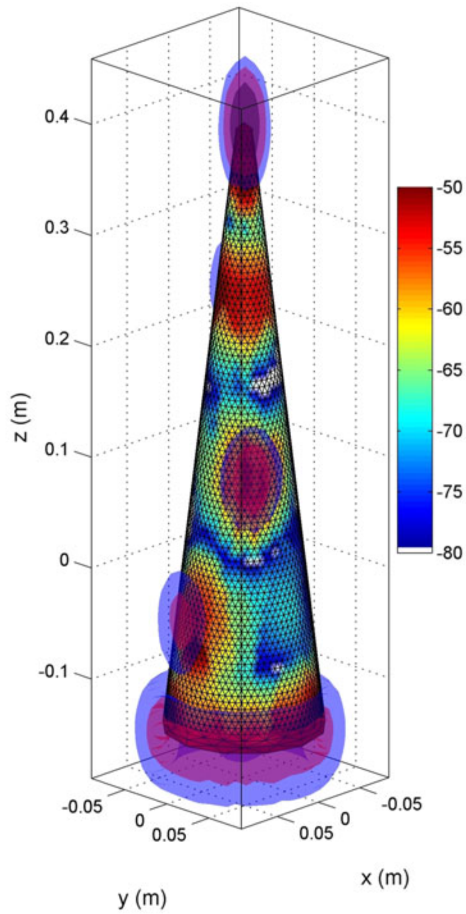

Fig. 12. 3-D radar map with conventional 3-D PFA
$[N = 256 \times 256 \times 512,\ M \approx 10^5]$.

of Fig. 11. There, the true patch locations are represented by black pellets. Note that although the creeping waves are not shown in Fig. 8, they would appear, under the cone, in other representations.

The application of conventional 3-D PFA imaging [6] to the concentric measurements is presented in Fig. 12. Here, all the measurements are taken into account as though the electric field remains constant. Similarly to the HHR imaging illustration of Section II, the reconstructed image mixes all the scatterers of various polarizations. Consequently, conventional 3-D PFA imaging, failing to distinguish the scatterers of Fig. 8 that express in polarization xx, cannot support a detailed and thorough RCS analysis. Remark that tomographic reconstruction, such as BP, would have given similar mixed results.

2) *Multiple Diffraction Artifacts & Polarization Dependence:* The second target is a metallic arrow 472 mm long and 150 mm large (it belongs to Airbus Group Innovation, see [34] for details). With such a target, diffraction edges are known to differ according to the polarization of the incident wave. Moreover, range-delayed multiple diffractions are likely to appear between the back of the arrow and its base.

Fig. 13 provides a comparison of 3-D radar maps of the arrow in polarization xx. Radar imaging from real data is compared to radar imaging from simulated data, computed with a parallelized 3-D EM solver (see [35] for details). It can be checked that both maps are very close one another. The sensitivity to wave polarization is emphasized in Figs. 13 and 14. The xx polarization map of Fig. 13 is again represented in the shape section of Fig. 15. Again, let us stress that the 3-D grid of the arrow shape is only represented for 3-D RCS analysis purpose and not at all in the inversion process. Depending on the polarization (i.e., xx, yy, or xy), the diffraction on the edges is more or less

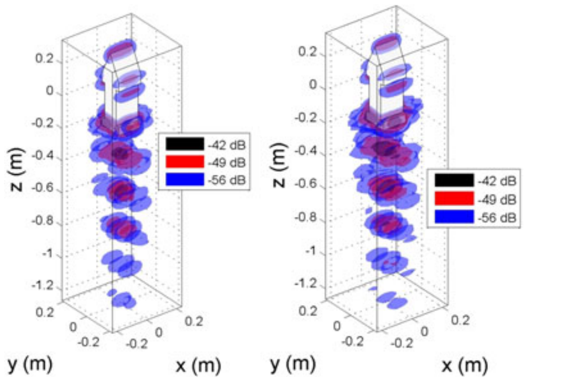

Fig. 13. 3-D radar image ($\widehat{\boldsymbol{s}}^{\mathrm{xx}}_{\mathrm{MNLS}}$) of the arrow, from real data (left) and simulated data (right) [$N = 40 \times 40 \times 1146$, $M \approx 4 \cdot 10^6$].

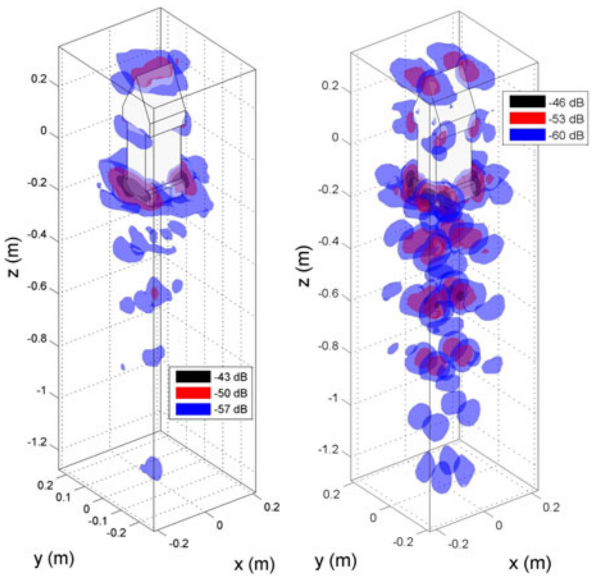

Fig. 14. 3-D radar image of the arrow (from real data): $\widehat{\boldsymbol{s}}^{\mathrm{yy}}_{\mathrm{MNLS}}$ (left) and $\widehat{\boldsymbol{s}}^{\mathrm{xy}}_{\mathrm{MNLS}}$ (right) [$N = 40 \times 40 \times 1146$, $M \approx 4 \cdot 10^6$].

important, as well as the range-delayed multiple reflections of the electromagnetic wave between the rear of the arrow and its base. Located below the target, they are much more important in $\widehat{\boldsymbol{s}}^{\mathrm{xx}}_{\mathrm{MNLS}}$ and $\widehat{\boldsymbol{s}}^{\mathrm{xy}}_{\mathrm{MNLS}}$, due to the higher resonance with the base. We should stress that the 3-D Radar imaging $\widehat{\boldsymbol{s}}^{\mathrm{xy}}_{\mathrm{MNLS}}$ enables us to localize not only 3-D scatterers associated with diffraction and reflexion but also scatterers that depolarize the incident wave, like the corners of the target. So the simultaneous determination of the three 3-D scatterer maps is particularly helpful for RCS analysis: it serves to localize and characterize each 3-D backscatterer.

Again, our radar imaging approach is compared to conventional 3-D PFA. For the arrow concentric measurements, conventional 3-D PFA leads to the 3-D image of Fig. 16. Again, the comparison to previous 3-D images of Figs. 13 and 14 shows that conventional PFA, considering all measurements without polarization distinction, mixes up the scatterers and provides an "average" image that is qualitatively and quantitatively inadequate for an accurate RCS analysis.

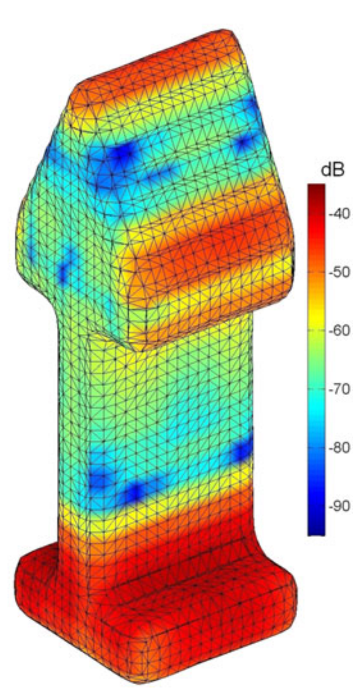

Fig. 15. 3-D radar image of the arrow: $\widehat{\boldsymbol{s}}^{\mathrm{xx}}_{\mathrm{MNLS}}$ (shape section) [$N = 40 \times 40 \times 1146$, $M \approx 4 \cdot 10^6$].

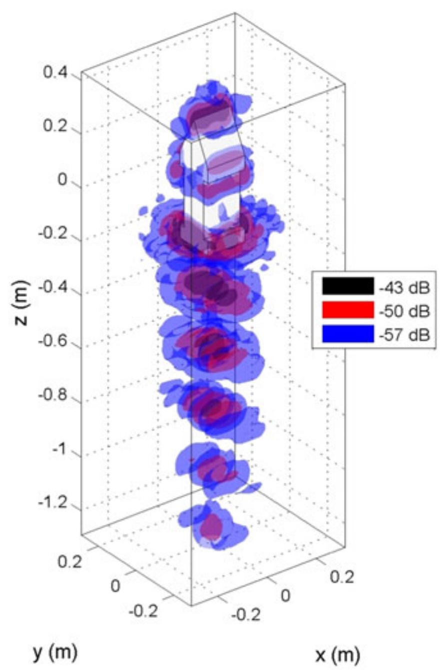

Fig. 16. 3-D radar map with conventional 3-D PFA [$N = 40 \times 40 \times 1146$, $M \approx 4 \cdot 10^6$].

V. CONCLUSION

A 3-D radar imaging technique has been presented. It is able to process collected scattered field data made of concentric measurements, where the electric field direction varies during the backscatter data acquisition. It is based on fast and efficient regularized inversion that integrates 3-D PFA and reconstructs three huge 3-D scatterer maps at a time from a single pass collection, whereas traditional algorithms unsuited to these concentric measurements would require two passes. It is applied successfully to synthetic and real data, collected from a 3-D spherical experimental layout dedicated to accurate RCS characterization.

To go further, the resolution could be enhanced by introducing nonquadratic approaches (L2-L1) [36], [37] or considering nondifferentiable criteria. From [38], constraints could be introduced, e.g., from the known shape, in order to improve the scatter inference and remove ambiguities [3]. Additionally, similarly to [2], [6], and [39], it could be possible to take into account the spherical near-field illumination of the target as well as the radiation pattern of the antenna.

APPENDIX A

MINIMUM NORM LEAST SQUARES

Consider the general quadratic problem in $\mathbb{C}^N$ with P linear equality constraints:

$$\widehat{\boldsymbol{x}} = \begin{cases} \arg\min_{\boldsymbol{x}\in\mathbb{C}^N} \|\boldsymbol{x}\|^2_{\boldsymbol{Q}} \\ \text{s.t. } \boldsymbol{c} - \boldsymbol{A}\boldsymbol{x} = 0 \end{cases} \tag{30}$$

where $\boldsymbol{Q}$ is a $N \times N$ positive-definite matrix that defines the criterion to be minimized while the constraint is described through the vector $\boldsymbol{c} \in \mathbb{C}^P$ and the $P \times N$ matrix $\boldsymbol{A}$. This matrix is assumed to be of full rank. A standard solution to such a problem relies on Lagrange theory: Lagrange multipliers, duality, and saddle point, as follows. The Lagrangian of the problem (30) reads:

$$\mathcal{L}(\boldsymbol{x}, \boldsymbol{u}) = \boldsymbol{x}^\dagger \boldsymbol{Q}\boldsymbol{x} + \boldsymbol{u}^\dagger(\boldsymbol{c} - \boldsymbol{A}\boldsymbol{x}) \tag{31}$$

where $\boldsymbol{u} \in \mathbb{C}^P$ is the Lagrange multiplier, also referred to as the dual variable ($\boldsymbol{x} \in \mathbb{C}^N$ is referred to as the primal variable).

Let us minimize $\mathcal{L}$ with respect to $\boldsymbol{x}$ (for a fixed $\boldsymbol{u}$) by setting to zero the gradient of the Lagrangian:

$$\frac{\partial \mathcal{L}}{\partial \boldsymbol{x}}(\bar{\boldsymbol{x}}, \boldsymbol{u}) = 2\boldsymbol{Q}\bar{\boldsymbol{x}} - \boldsymbol{A}^\dagger \boldsymbol{u} = 0.$$

The solution is directly given by

$$\bar{\boldsymbol{x}} = \frac{1}{2}\boldsymbol{Q}^{-1}\boldsymbol{A}^\dagger \boldsymbol{u}\,. \tag{32}$$

Note that the Hessian is equal to $2\boldsymbol{Q}$ and hence is strictly positive. Consequently, $\bar{\boldsymbol{x}}$ corresponds to a minimum. Then, the introduction of its value in the expression of $\mathcal{L}$ given by (31) provides the dual function $\bar{\mathcal{L}}$:

$$\bar{\mathcal{L}}(\boldsymbol{u}) = \inf_{\boldsymbol{x}} \mathcal{L}(\boldsymbol{x}, \boldsymbol{u}) = \mathcal{L}(\bar{\boldsymbol{x}}, \boldsymbol{u}) = -\frac{1}{4}\boldsymbol{u}^\dagger \boldsymbol{A}\boldsymbol{Q}^{-1}\boldsymbol{A}^\dagger \boldsymbol{u} + \boldsymbol{u}^\dagger \boldsymbol{c}\,.$$

Next, let us maximize $\bar{\mathcal{L}}(\boldsymbol{u})$ relatively to $\boldsymbol{u}$ by also setting to zero the gradient with respect to the dual variable:

$$0 = \frac{\partial \bar{\mathcal{L}}}{\partial \boldsymbol{u}}(\bar{\boldsymbol{u}}) = -\frac{1}{2}\boldsymbol{A}\boldsymbol{Q}^{-1}\boldsymbol{A}^\dagger \bar{\boldsymbol{u}} + \boldsymbol{c}.$$

The solution is directly given by

$$\bar{\boldsymbol{u}} = 2(\boldsymbol{A}\boldsymbol{Q}^{-1}\boldsymbol{A}^\dagger)^{-1}\boldsymbol{c}\,. \tag{33}$$

Note that the Hessian is equal to $-(\boldsymbol{A}\boldsymbol{Q}\boldsymbol{A}^\dagger)/2$ and hence is strictly negative; $\bar{\boldsymbol{u}}$ corresponds to a maximum. Let us insert the expression (33) of the dual optimizer into the expression (32) of the primal optimizer. It leads to

$$\widehat{\boldsymbol{x}} = \boldsymbol{Q}^{-1}\boldsymbol{A}^\dagger(\boldsymbol{A}\boldsymbol{Q}^{-1}\boldsymbol{A}^\dagger)^{-1}\boldsymbol{c} \tag{34}$$

which is the MNLS solution. When $\boldsymbol{Q}$ is the identity matrix, it results in the expression (28):

$$\widehat{\boldsymbol{x}} = \boldsymbol{A}^\dagger(\boldsymbol{A}\boldsymbol{A}^\dagger)^{-1}\boldsymbol{c}\,.$$

Note that, if $N = P$, $\boldsymbol{A}$ is invertible and $\widehat{\boldsymbol{x}} = \boldsymbol{A}^{-1}\boldsymbol{c}$.

APPENDIX B

3-D PFA IMAGING AS A MNLS SOLUTION

For classical radar imaging collection of Fig. 2, only one of the three scattering coefficients intervenes, depending on the acquisition mode (HH, VV, or HV). The direct model (22) of Section III then involves only one vector $\boldsymbol{s}$:

$$\boldsymbol{\mathcal{S}} = \boldsymbol{A}\boldsymbol{s} + \boldsymbol{\varepsilon} \tag{35}$$

where $\boldsymbol{s} = [s_1 \quad s_2 \quad \cdots \quad s_N]^{\mathrm{t}}$ is the unknown vector map associated to the chosen polarization, $\boldsymbol{A} = \boldsymbol{T}\boldsymbol{F}$ is a matrix of size $M \times N$ and $\boldsymbol{\varepsilon}$ is the noise vector.

Then, from expression (28) demonstrated in Appendix A, the MNLS solution can be expressed by

$$\widehat{\boldsymbol{s}}_{\text{MNLS}} = \boldsymbol{A}^\dagger(\boldsymbol{A}\boldsymbol{A}^\dagger)^{-1}\boldsymbol{\mathcal{S}} = (\boldsymbol{T}\boldsymbol{F})^\dagger[\boldsymbol{T}\boldsymbol{F}(\boldsymbol{T}\boldsymbol{F})^\dagger]^{-1}\boldsymbol{\mathcal{S}}\,. \tag{36}$$

After simplification, the MNLS solution is given by

$$\widehat{\boldsymbol{s}}_{\text{MNLS}} = \boldsymbol{F}^\dagger\boldsymbol{T}^{\mathrm{t}}\boldsymbol{\mathcal{S}}\,.$$

The MNLS solution $\widehat{\boldsymbol{s}}_{\text{MNLS}}$ is obtained by IFFT of the zero-padded weighted measurements. In this imaging context, it is known as the 3-D PFA algorithm [4]. Here, the regridding step is achieved by the mean of the truncation matrix $\boldsymbol{T}$ ($\boldsymbol{T}^{\mathrm{t}}$ being the zero-padding matrix). Note that 3-D PFA does not provide the MNLS solution if another interpolation scheme, such as linear or cubic, is used.

REFERENCES

[1] J. Pinto, J. Matthews, and G. Sarno
Stealth technology for wind turbines
IET Radar, Sonar Navig., vol. 4, no. 1, pp. 126–133, 2010.

[2] J. Fortuny and A. J. Sieber
Three-dimensional synthetic aperture radar imaging of a fir tree: First results
IEEE Trans. Geosci. Remote Sens., vol. 37, no. 2, pp. 1006–1014, Mar. 1999.

[3] D. L. Mensa
High Resolution Radar Cross-Section Imaging, vol. 1, Boston, MA, USA: Artech House, 1991, p. 280.

[4] J. M. Lopez-Sanchez and J. Fortuny-Guasch
3-d radar imaging using range migration techniques
IEEE Trans. Antennas Propag., vol. 48, no. 5, pp. 728–737, May 2000.

[5] C. V. Jakowatz, D. E. Wahl, P. H. Eichel, D. C. Ghiglia, and P. A. Thompson
Spotlight-Mode Synthetic Aperture Radar: A Signal Processing Approach: A Signal Processing Approach. New York, NY, USA: Springer, 2012.

[6] J. Fortuny
An efficient 3-d near-field ISAR algorithm
IEEE Trans. Aerosp. Electron. Syst., vol. 34, no. 4, pp. 1261–1270, Oct. 1998.

[7] C. Ozdemir
Inverse Synthetic Aperture Radar Imaging with MATLAB Algorithms, vol. 210. Hoboken, NJ, USA: Wiley, 2012.

[8] K. Knaell and G. Cardillo
Radar tomography for the generation of three-dimensional images
Proc. Inst. Elect. Eng. Radar, Sonar Navig., vol. 142, no. 2, pp. 54–60, 1995.

[9] K. E. Dungan and L. C. Potter
3-d imaging of vehicles using wide aperture radar
IEEE Trans. Aerosp. Electron. Syst., vol. 47, no. 1, pp. 187–200, Jan. 2011.

[10] M. Martorella, D. Stagliano, F. Salvetti, and N. Battisti
3d interferometric ISAR imaging of noncooperative targets
IEEE Trans. Aerosp. Electron. Syst., vol. 50, no. 4, pp. 3102–3114, Oct. 2014.

[11] L. Zhao, M. Gao, M. Martorella, and D. Stagliano
Bistatic three-dimensional interferometric ISAR image reconstruction
IEEE Trans. Aerosp. Electron. Syst., vol. 51, no. 2, pp. 951–961, Apr. 2015.

[12] X. Xu and R. M. Narayanan
Three-dimensional interferometric ISAR imaging for target scattering diagnosis and modeling
IEEE Trans. Image Process., vol. 10, no. 7, pp. 1094–1102, Jul. 2001.

[13] J. Mayhan, M. Burrows, K. Cuomo, and J. Piou
High resolution 3d snapshot ISAR imaging and feature extraction
IEEE Trans. Aerosp. Electron. Syst., vol. 37, no. 2, pp. 630–642, Apr. 2001.

[14] P. Massaloux and P. Bérisset
Achieved mechanical accuracy of a 3d RCS spherical near field arch positioning system
In *Proc. Annu. Meeting Antenna Meas. Techn. Assoc.*, 2012.

[15] P. Massaloux, G. Cartesi, P. Bérisset, and M. Mognot
Indoor RCS measurement facility arche 3d: Influence of the target supporting mast
In *Proc. Annu. Meeting Antenna Meas. Techn. Assoc.*, 2014.

[16] P. Massaloux, M. Mognot, G. Mazé-Merceur, and M. Sesques
Impact of the target supporting mast in an indoor RCS measurement facility: Computation and measurement
In *Proc. Eur. Conf. Antenna Propag.*, 2015, pp. 1–4.

[17] C. Eyraud
Validation of a 3d bistatic microwave scattering measurement setup
Radio Sci., vol. 43, no. 4, pp. 1–12, 2008.

[18] D. Escot, D. Poyetos, J. Aguilar, I. Montiel, I. Gonzalez, and F. S. De Adana
Indoor 3D full polarimetric bistatic spherical facility for electromagnetic tests
IEEE Antennas Propag. Mag., vol. 52, no. 4, pp. 112–118, Aug. 2010.

[19] P. Massaloux, P. Minvielle, and J.-F. Giovannelli
Indoor 3D spherical near field RCS measurement facility: Localization of scatterers
In *Proc. 8th Eur. Conf. Antennas Propag.*, 2014, pp. 2765–2769.

[20] E. F. Knott, J. F. Shaeffer, and M. T. Tuley
Radar Cross Section. Norwood, MA, USA: Artech House, 1993.

[21] M. Cheney and B. Borden
Fundamentals of Radar Imaging. Philadelphia, PA, USA: SIAM, 2009, vol. 79.

[22] E. F. Knott
Radar Cross Section Measurements. Raleigh, NC, USA: SciTech Publishing, 2006.

[23] J.-S. Lee and E. Pottier
Polarimetric Radar Imaging: From Basics to Applications. Boca Raton, FL, USA: CRC, 2009.

[24] H. A. Zebker and J. J. Van Zyl
Imaging radar polarimetry: A review
Proc. IEEE, vol. 79, no. 11, pp. 1583–1606, Nov. 1991.

[25] J.-F. Giovannelli and J. Idier, Eds.
Regularization and Bayesian Methods for Inverse Problems in Signal and Image Processing. London, U.K.: ISTE Ltd., 2015.

[26] M. Bertero and P. Boccacci
Introduction to Inverse Problems in Imaging. New York, USA: Taylor & Francis, 2002.

[27] B. Chalmond
Modeling and Inverse Problems in Image Analysis (Series Applied Mathematical Science). New York, NY, USA: Springer, 2003.

[28] J. Kaipio and E. Somersalo
Statistical and Computational Inverse Problems. Berlin, Germany: Springer, 2005.

[29] R. C. Aster, B. Borchers, and C. H. Thurber
Parameter Estimation and Inverse Problems (Series International Geophysics Series). Amsterdam, The Netherlands: Elsevier, 2005.

[30] M. Soumekh
Synthetic Aperture Radar Signal Processing. Hoboken, NJ, USA: Wiley, 1999.

[31] P. Massaloux, G. Cartesi, and D. Lespiaux
Indoor RCS measurement facility arche 3D: RCS multi-calibration under spherical wave
In *Proc. Annu. Meeting Antenna Meas. Techn. Assoc.*, 2015, pp. 1–5.

[32] A. C. Woo and all
EM programmer's notebook-benchmark radar targets for the validation of computational electromagnetics programs
IEEE Antennas Propag. Mag., vol. 35, no. 1, pp. 84–89, Feb. 1993.

[33] F. Giraud, P. Minvielle, and P. Del Moral
Advanced interacting sequential Monte Carlo sampling for inverse scattering
Inverse Problems, vol. 29, no. 9, 2013, Art. no. 095014.

[34] J. Castelli
National comparison of radar cross section measurements: Motivations and scheduled tasks
In *Proc. IEEE Conf. Antenna Meas. Appl.*, 2014, pp. 1–4.

[35] C. Augonnet, D. Goudin, A. Pujols, and M. Sesques
Accelerating a massively parallel numerical simulation in electromagnetism using a cluster of GPUs
In *Parallel Processing and Applied Mathematics*. New York, NY, USA: Springer, 2014, pp. 593–602.

[36] M. Çetin and W. C. Karl
Feature-enhanced synthetic aperture radar image formation based on nonquadratic regularization
IEEE Trans. Image Process., vol. 10, no. 4, pp. 623–631, Apr. 2001.

[37] R. Boubertakh, J.-F. Giovannelli, A. D. Cesare, and A. Herment
Non-quadratic convex regularized reconstruction of MR images from spiral acquisitions
Signal Process., vol. 86, no. 9, pp. 2479–2494, 2006.

[38] J.-F. Giovannelli and A. Coulais
Positive deconvolution for superimposed extended source and point sources
Astron. Astrophys., vol. 439, no. 1, pp. 401–412, Aug. 2005.

[39] A. Broquetas, J. Palau, L. Jofre, and A. Cardama
Spherical wave near-field imaging and radar cross-section measurement
IEEE Trans. Antennas Propag., vol. 46, no. 5, pp. 730–735, May 1998.

Pierre Minvielle was born in Madrid, Spain, in 1969. He received the Dipl. Ing. degree from the École Nationale Supérieure d'Informatique et de Mathématiques Appliquées de Grenoble, France, in 1992 and, at the same time, the M.Sc. degree in probability and statistics from the University Joseph Fourier of Grenoble, Saint-Martin d'Hères, France.

He joined the French Atomic Energy Commission, in 1997, where he has worked on operational analysis, data processing and applied statistics. In 2003, he was on secondment at QinetiQ Ltd. (Malvern, U.K.), working on sequential Monte Carlo methods for target tracking and recognition. Since 2010, he has been working on uncertainty quantification and predictive simulation. In 2013, he spent one year with the Advanced Learning Evolutionary Algorithms team of the French National Institute for Research in Computer Science and Control (INRIA), Talence, France, dealing with advanced Monte Carlo inference methods. His current interests are computational statistics and inverse problems.

Pierre Massaloux was born in Limoges, France, in 1984. He received the Dipl. Ing. degree from the Ecole d'Ingénieurs en Génie Electrique, Rouen, France, in 2007.

In 2007, he joined the French Atomic Energy Commission), where he is responsible for RCS measurement technical facilities. His research interests include radar cross section and antenna measurements techniques, signal processing, antenna design, and radar imaging.

Jean-François Giovannelli was born in Béziers, France, in 1966. He received the Dipl. Ing. degree from the École Nationale Supérieure de l'Électronique et de ses Applications, Cergy, France, in 1990, and the Ph.D. degree and the H.D.R. degree in signal-image processing from the Université Paris-Sud, Orsay, France, in 1995 and 2005, respectively.

From 1997 to 2008, he was an Assistant Professor with the Université Paris-Sud and a Researcher with the Laboratoire des Signaux et Systèmes, Groupe Problèmes Inverses. He is currently a Professor with the Université de Bordeaux, France and a Researcher with the Laboratoire de l'Intégration du Matériau au Système, Groupe Signal-Image, France. His research focuses on inverse problems in signal and image processing, mainly unsupervised and myopic problems. From a methodological standpoint, the developed regularization methods are both deterministic (penalty, constraints,...) and Bayesian. Regarding the numerical algorithms, the work relies on optimization and stochastic sampling. His application fields essentially concern astronomical, medical, proteomics, radars and geophysical imaging.